



Experimental evidence of enhanced ferroelectricity in Ca doped BiFeO₃



L.V. Costa ^{a,1}, R.C. Deus ^{a,1}, C.R. Foschini ^{b,1}, E. Longo ^{b,1}, M. Cilense ^{c,2}, A.Z. Simões ^{a,*}

^a Universidade Estadual Paulista, UNESP, Faculdade de Engenharia de Guaratinguetá, Av. Dr. Ariberto Pereira da Cunha, 333, Bairro Portal das Colinas, CEP 12516-410 Guaratinguetá, SP, Brazil

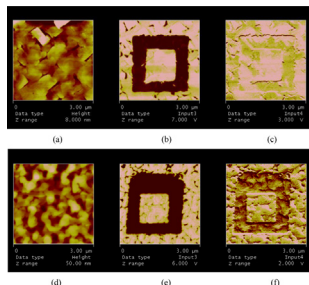
^b Universidade Estadual Paulista, UNESP, Faculdade de Engenharia de Bauru, Dept. de Eng. Mecânica, Av. Eng. Luiz Edmundo C. Coube 14-01, 17033-360 Bauru, SP, Brazil

^c Universidade Estadual Paulista, UNESP, Instituto de Química – Laboratório Interdisciplinar em Cerâmica (LIEC), Rua Professor Francisco Degni s/n, 14800-90 Araraquara, SP, Brazil

HIGHLIGHTS

- Ca doped BiFeO₃ thin films were obtained by the polymeric precursor method.
- Co-existence of distorted rhombohedral and tetragonal phases are evident.
- Enhanced ferroelectric and piezoelectric properties are produced by the internal strain in the Ca doped BiFeO₃ film.

GRAPHICAL ABSTRACT



ARTICLE INFO

Article history:

Received 14 June 2013

Received in revised form

15 October 2013

Accepted 12 January 2014

Keywords:

- A. Ceramics
A. Thin films
B. Coatings
B. Chemical synthesis

ABSTRACT

Calcium (Ca)-doped bismuth ferrite (BiFeO₃) thin films prepared by using the polymeric precursor method (PPM) were characterized by X-ray diffraction (XRD), field emission gun scanning electron microscopy (FEG-SEM), transmission electron microscopy (TEM), polarization and piezoelectric measurements. Structural studies by XRD and TEM reveal the co-existence of distorted rhombohedral and tetragonal phases in the highest doped BiFeO₃ where enhanced ferroelectric and piezoelectric properties are produced by internal strain. Resistive switching is observed in BFO and Ca-doped BFO which are affected by the barrier contact and work function of multiferroic materials and Pt electrodes. A high coercive field in the hysteresis loop is observed for the BiFeO₃ film. Piezoelectric properties are improved in the highest Ca-doped sample due to changes in the crystal structure of BFO for a primitive cubic perovskite lattice with four-fold symmetry and a large tetragonal distortion within the crystal domain. This observation introduces magnetoelectronics at room temperature by combining electronic conduction with electric and magnetic degrees of freedom which are already present in the multiferroic BiFeO₃.

© 2014 Elsevier B.V. All rights reserved.

1. Introduction

Multiferroic materials with ferroelectric and ferromagnetic simultaneous ordering are currently attracting significant attention due to their interesting fundamental physics as well as their potential applications [1–5]. Among the single-phase multiferroic materials studied, BiFeO₃ (BFO) with a rhombohedrally distorted

* Corresponding author. Tel.: +55 12 3123 2228.

E-mail address: alezipo@yahoo.com (A.Z. Simões).

¹ Tel.: +55 12 3123 2228.

² Tel.: +55 16 3301 9828.

perovskite structure and a space group of R3c is the only material which exhibits both ferroelectricity and G-type antiferromagnetism at room temperature (with a Curie temperature T_c of 1103 K and Néel temperature T_N of 643 K) which facilitates applications at room temperature [6–8]. However, pure BFO has a serious high leakage current problem resulting from charge defects such as oxygen vacancies and the cancellation of ion magnetic moments due to its spatial periodic inhomogeneous spin structure [9] which hinders its practical applications in multiferroic devices. Considerable efforts have been expended to improve BFO properties; e.g., A-site substitution with La^{3+} , Nd^{3+} , Ce^{3+} and Tb^{3+} [10–15] and B-site substitution with Ni^{2+} , Cu^{2+} , Co^{2+} , Cr^{3+} , Mn^{3+} , Ti^{4+} , Zr^{4+} and V^{5+} [16–18] etc. These studies confirmed that ion doping is an effective method to improve BFO properties. Since BFO ferroelectricity of BFO evolves from a lone pair of A-site Bi^{3+} ion electrons [3–5], ferroelectric property effects are very important [19,20]. Ramesh et al. studied the quasi-non-volatile and reversible modulation of electric conduction accompanied by the modulation of the ferroelectric state in Ca-doped BiFeO_3 films using an electric field as the control parameter. The mechanism of this modulation in Ca-doped BiFeO_3 is based on electronic conduction as a consequence of naturally produced oxygen vacancies that act as donor impurities to compensate Ca acceptors and maintain a highly stable Fe^{3+} valence state [21]. For the low Ca doping regime ($x < 0.1$), films with a monoclinic structure undergo a first-order transition to a pseudo-tetragonal phase at higher temperatures with a thermal hysteresis. The extrapolation of the transition temperature results in the well known ferroelectric Curie temperature (T_c) of BiFeO_3 at 1100 K. With increased Ca doping, the ferroelectric T_c rapidly decreases, and a T_c of 600 K with a thermal hysteresis of 240 K is recorded. It has been reported that the T_c of some ferroelectrics such as BaTiO_3 and PbTiO_3 is very sensitive to the strain state [22,23]. However, because BiFeO_3 ferroelectricity is primarily attributed to Bi 6s lone-pair electrons, ferroelectric properties and the T_c are expected to be less sensitive to strain [24]. However, a number of studies related to this phenomenon have been reported. Therefore, for this paper, we prepared A-site Ca-doped BFO films with different compositions on Pt/Ti/SiO₂/Si substrates by using the PPM and investigated their influence on the structure, microstructure and ferro/piezoelectric properties.

2. Experimental procedure

Ca-modified BiFeO_3 thin films were prepared by the PPM as described elsewhere [25]. Films were spin coated on Pt/Ti/SiO₂/Si substrates by a commercial spinner operating at 5000 revolutions/min for 30 s (spin coater KW-4B, Chemat Technology). An excess of 5% wt of Bi was added to the solution to minimize bismuth loss during thermal treatment. Thin films were annealed at 500 °C for 2 h in a conventional furnace under static air atmosphere. The film thickness was reached by repeating spin-coating and heating treatment cycles ten times. Annealed film thicknesses were measured using SEM (Topcom SM-300) at the transversal section. We have obtained films with thicknesses in the range of 340–360 nm. A phase analysis of films was performed at room temperature by XRD using a Bragg-Brentano diffractometer (Rigaku 2000) and CuK α radiation; in this case, back scattering electrons were used. The Rietveld analysis was performed with the Rietveld refinement program DBWS-941 1 [26]. The profile function used was the modified Thompson-Cox-Hastings pseudo-Voigt where η (the Lorentzian fraction of the function) varies with the Gauss and Lorentz components of the full width at half maximum. The morphology of the films was observed using a high resolution FEG-SEM (Supra 35-VP, Carl Zeiss, Germany). To obtain better insight into the nature of the deposited phases and their crystallographic

relationship, cross-sectional samples from different films were further investigated by TEM and selected area diffraction (SAD) patterns onto 300 mesh Cu grids. Measurements were then taken at an accelerating voltage of 200 kV on a Philips model CM 200 instrument. Top Au electrodes (0.5 mm diameter) were prepared for electrical measurements by evaporation through a shadow mask at room temperature. The current–voltage characteristic was determined with an ammeter (Keithley 6430) with a 10 μA current compliance (used here to prevent permanent damage on films). Piezoelectric measurements were carried out using a set-up based on an atomic force microscope in a multimode scanning probe microscope with a nanoscope IV controller (Veeco FPP-100). In our experiments, piezoresponse images of films were acquired in ambient air by applying a small ac voltage with an amplitude of 2.5 V (peak to peak) and a frequency of 10 kHz while scanning the film surface. To apply the external voltage, we used a standard gold-coated Si₃N₄ cantilever with a spring constant of 0.09 N m⁻¹. With an apex radius of about 20 nm, the probing tip was in mechanical contact with the uncoated film surface during measurements. Cantilever vibration was detected using a conventional lock-in technique. Ferroelectric properties of the capacitor were measured on a Radiant Technology RT6000 instrument and a tester equipped with a micrometer probe station in a virtual ground mode at a frequency of 60 Hz. These loops were traced using the Charge 5.0 program included in the software of the RT6000HVS in a virtual ground mode test device. All measurements were taken at room temperature.

3. Results and discussion

Fig. 1 illustrates XRD patterns of BFO and Ca-doped BFO films deposited on platinum-coated silicon substrates. The films were well crystallized at a processing temperature of 500 °C. BFO and Ca-doped BFO films self-organized to produce (110)-preferred orientation with good crystallinity. With partial substitution of Ca ions for A-site bismuth ions, the BCFO film (108) diffraction peak shifted toward a higher angle. No additional peak related to CaO could be assigned by revealing partial substitution of Ca by bismuth in the crystal lattice and solid solution of Ca substitution in BFO. The BCF030 film has a tetragonal structure with a $P4mm$ space group while BFO has a rhombohedral structure with a R3c space group which can be treated as a special triclinic structure [14]. To verify and confirm the structure of BCFO thin films a structural refinement by the Rietveld method was performed. The Rietveld method is a

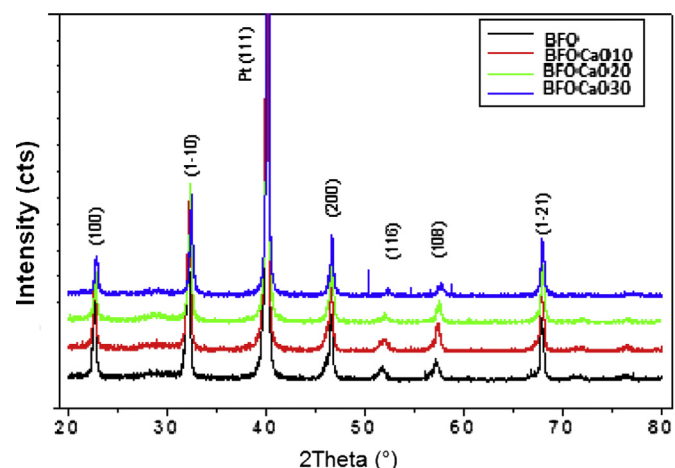


Fig. 1. X-ray diffraction of BFO, BFO:Ca010, BFO:Ca020, BFO:Ca030 thin films deposited by the polymeric precursor method and annealed at 500 °C in static air for 2 h.

Table 1

Index refinements for BFO, BFOCa010, BFOCa020 and BFOCa030 thin films annealed at 500° for 2 h.

	Parameter	BFO	BFOCa010	BFOCa020	BFOCa030
Refinement index	R_{wp} (%)	8.14	5.97	5.51	4.59
	R_{exp}	4.67	3.91	3.76	3.31
	S	1.74	1.52	1.46	1.38
Atomic Positions	A1	0; 0; 0.06722	0; 0; 0.06712	0; 0; 0.06720	0; 0; 0.06733
	A2	0; 0; 0.21091	0; 0; 0.21023	0; 0; 0.21132	0; 0; 0.21145
	B1	0; 0; $\frac{1}{2}$	0; 0; $\frac{1}{2}$	0; 0; $\frac{1}{2}$	0; 0; $\frac{1}{2}$
	B2	0; 0; 0.37099	0; 0; 0.37213	0; 0; 0.37143	0; 0; 0.37120
	O1	$\frac{1}{4}$; $\frac{1}{4}$; 0	$\frac{1}{4}$; $\frac{1}{4}$; 0	$\frac{1}{4}$; $\frac{1}{4}$; 0	$\frac{1}{4}$; $\frac{1}{4}$; 0
	O2	$\frac{1}{4}$; $\frac{1}{4}$; $\frac{1}{4}$	$\frac{1}{4}$; $\frac{1}{4}$; $\frac{1}{4}$	$\frac{1}{4}$; $\frac{1}{4}$; $\frac{1}{4}$	$\frac{1}{4}$; $\frac{1}{4}$; $\frac{1}{4}$
	O3	0; 0; 0.43786	0; 0; 0.43747	0; 0; 0.43616	0; 0; 0.43638
	O4	0; 0; 0.32536	0; 0; 0.31851	0; 0; 0.31895	0; 0; 0.31989
	O5	$\frac{1}{4}$; $\frac{1}{4}$; 0.11165	$\frac{1}{4}$; $\frac{1}{4}$; 0.11584	$\frac{1}{4}$; $\frac{1}{4}$; 0.11580	$\frac{1}{4}$; $\frac{1}{4}$; 0.11581
S_{occ}	Bi (A1)	1.00000	0.87500	0.75000	0.62500
	Ca (A1)	0.00000	0.12500	0.25000	0.37500
	O	0.91700	0.91000	0.91800	0.94900
Lattice Parameter	a (Å)	5.577352	5.576058	5.577687	5.578439
	c (Å)	13.867785	13.807185	13.773235	13.764944
	V (Å ³)	373.529	371.784	371.086	370.963
Perovskite (mol%)	t	0.915	0.916	0.919	0.920
		97.5 ± 0.5	97.1 ± 0.4	98.4 ± 0.4	97.7 ± 0.4
	Stoichiometry	BiFeO ₃	Bi _{0.9} Ca _{0.1} FeO ₃	Bi _{0.80} Ca _{0.2} FeO ₃	Bi _{0.70} Ca _{0.30} FeO ₃
Refinement		BiFeO _{2.6}	Bi _{0.9} Ca _{0.1} FeO _{2.6}	Bi _{0.80} Ca _{0.2} FeO _{2.6}	Bi _{0.70} Ca _{0.30} FeO _{2.8}

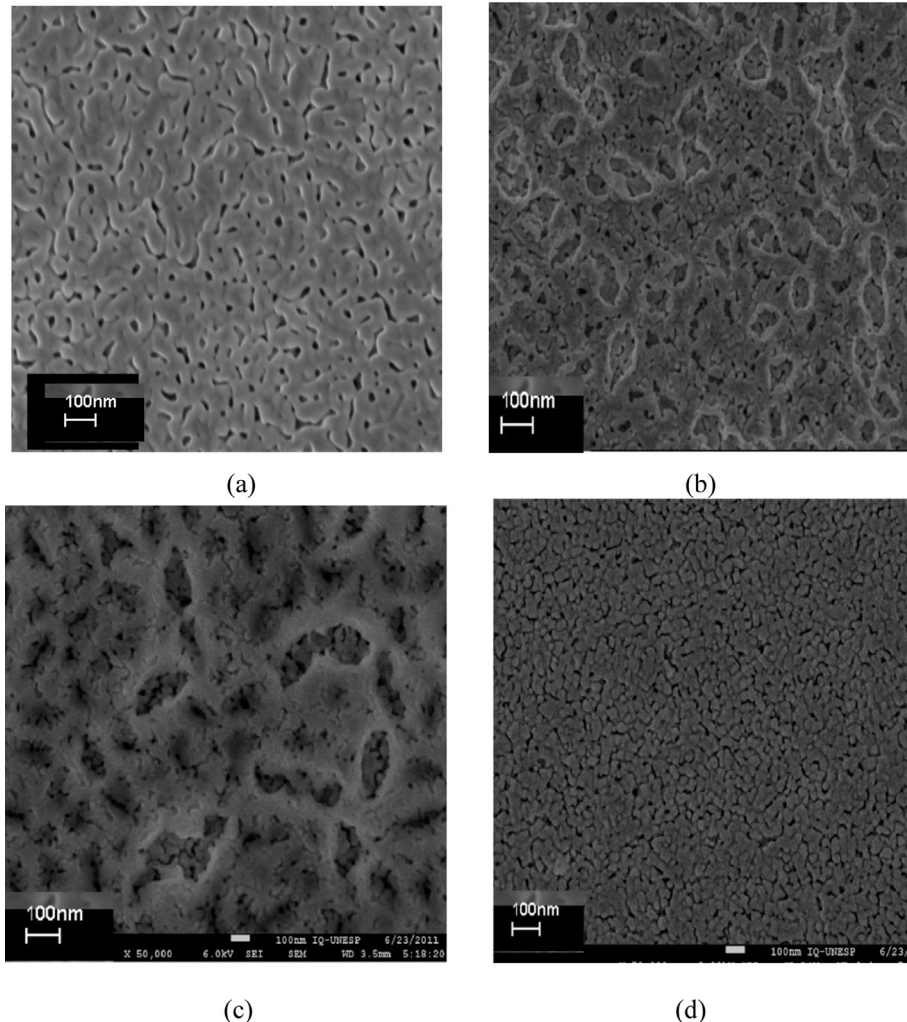


Fig. 2. FEG-SEM micrograph of thin films deposited by the polymeric precursor method and annealed at 500 °C in static air for 2 h. (a) BFO, (b) BFOCa010, (c) BFOCa020 and (d) BFOCa030.

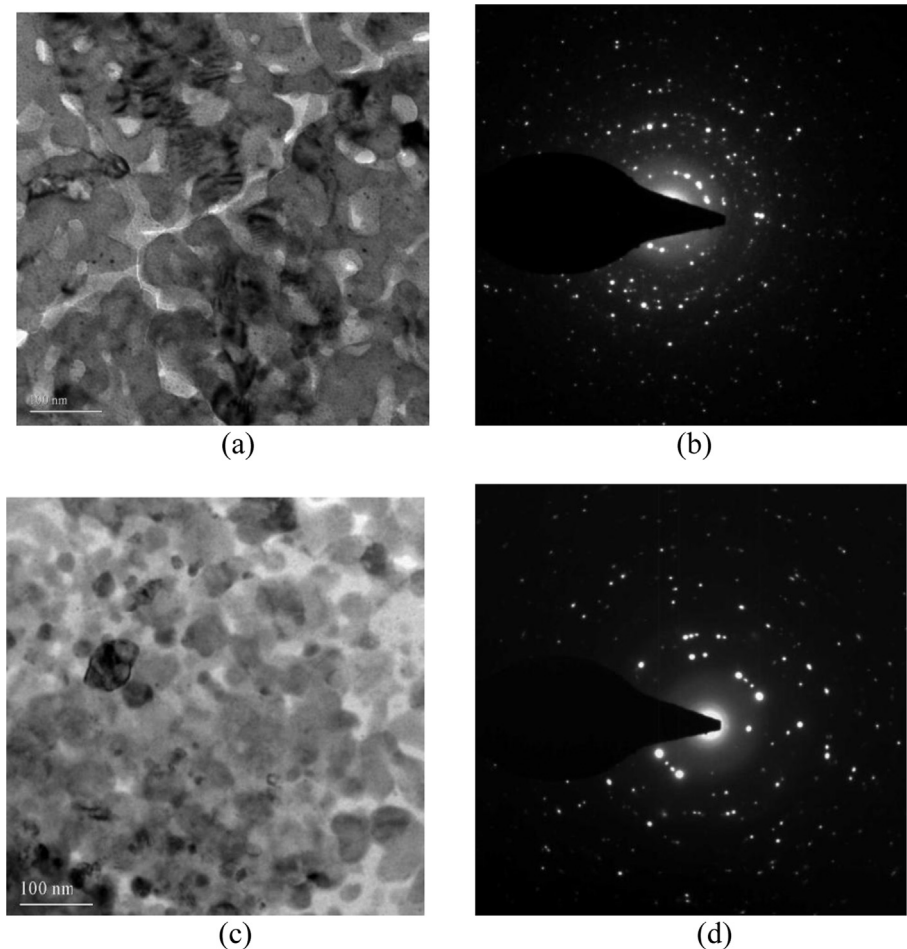


Fig. 3. TEM and SAD microographies of thin films deposited by the polymeric precursor method and annealed at 500 °C in static air for 2 h. (a) BFO (TEM), (b) BFO (SAD), (c) BFOCa030 (TEM) and (d) BFOCa030 (SAD).

least squares refinement procedure where the experimental step-scanned values are adapted to calculated values. The profiles are considered to be known, and a model for a crystal structure is available [27]. This structural refinement method presents several advantages over conventional quantitative analysis methods because this method uses a whole pattern fitting algorithm where all lines for each phase are explicitly considered, and even severely overlapped lines are usually not a problem. Thus, it is not necessary to decompose patterns into separate Bragg peaks as is often the case for traditional methods. The use of all reflections in a pattern rather than just the strongest reflections minimizes both uncertainty in derived weight fractions and effects of preferred orientation, primary extinction and nonlinear detection systems [28]. The structural refinement was performed by using a Maud program [29] which employs the Rietveld texture and stress analysis [30]. According to the literature [31,32], the quality of data from structural refinement is generally checked by R -values (R_{wp} , R_{exp} , and S). The quality of structural refinement also can be verified by the R_{wp} factor value. Its absolute value does not depend on the absolute value of the intensities; instead it depends on the background with a high background, it is easier to reach very low values. Increasing the number of peaks (sharp peaks) created more difficulty in obtaining a good value. Structural refinement data are acceptable when the R_{wp} is $<10\%$ for a medium complex phase, when high complex phases (monoclinic to triclinic), have a value of $R_{wp} < 15\%$ and when a highly symmetric material or compound (cubic) with few peaks has a value of $R_{wp} < 8\%$ [33].

Table 1 lists R_{wp} , R_{exp} , and S indexes as well as lattice parameters (a and c) and the unit cell volume (V). Atomic positions obtained by Rietveld analyses belong to the ICSD card (86-1518). Quantitative phase analyses of powders for the rhombohedral phase were calculated according to Young and Wiles [26]. Results obtained confirm that the Bi^{+3} ion was substituted by the Ca^{+2} ion in the rhombohedral BFO phase, and no changes occurred in refinements. Ca^{+2} substitutes for Bi^{+3} only in a perovskite-type unit cell which causes a distorted structure whereby distortion increases with a higher Ca content. The covalent interaction which originates from the strong hybridization between Fe 3d and O 2p orbitals plays an important role in the structural distortion of the BFO lattice. Doping with Ca improves oxygen ion stability in the lattice because some of the Bi ions in the pseudo-perovskite layers containing Fe–O octahedra are substituted by the rare earth ion. From low S values ($S = R_{wp}/R_{exp}$), it can be assumed that the refinement was successfully performed with all the investigated parameters close to literature data [34]. It can be inferred that the c -axis is less elongated after Ca addition which is caused by differences in charge densities of Ca and bismuth atoms. Also, the addition of Ca has a radial substitution effect higher than bismuth and stabilizes oxygen vacancies and consequently the structure. The decrease in the lattice parameter and unit cell volume is almost linear as expected due to the stoichiometric replacement of Bi^{+3} with a smaller ionic radii substituent (in this case Ca^{+2}).

The results obtained from the structural refinement are displayed in **Table 1**. In this table, the fitting parameters (R_{wp} , R_{exp} , and

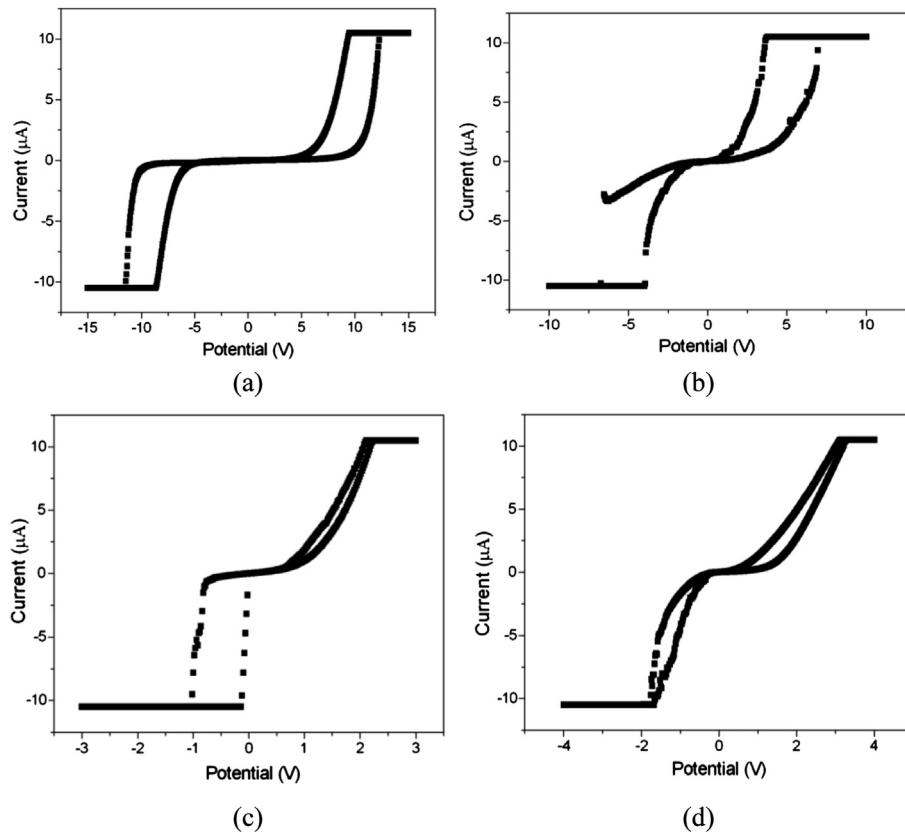


Fig. 4. Typical I - V hysteresis curve of thin films deposited by the polymeric precursor method and annealed at 500 °C in static air for 2 h. (a) BFO, (b) BFOCa010, (c) BFOCa020 and (d) BFOCa030.

S) indicate good agreement between refined and observed XRD patterns. Small variations in lattice parameters, unit cell volumes and displacements on Fe atoms (network formers) are indicative of distortions/strain in the lattice caused by differences in crystal lattice parameters and the thermal expansion behavior between the film and the underlying substrate or arising from defects promoted by $[BiO_{12}]$ and $[CaO_{12}]$ clusters (network modifiers).

FEG-SEM was used to confirm the surface morphology (see Fig. 2). Changes in the surface of the Ca-doped BFO films were evaluated; and the results reveal that the BCF030 film consists of a homogeneous surface although BFO film has a degree of porosity. It was also found that the Ca dopant tends to suppress grain growth. BCF030 was found to be effective in improving the surface morphology of synthesized BFO-based films because the precursor film underwent the optimized nucleation and growth process to produce films with a homogeneous and dense microstructure. On the other hand, for low and middle Ca concentrations, the surface consists of irregularities which were caused by distortion and strain influenced by differences in the thermal expansion coefficient of the multiferroic material and the substrate. The average grain size is 63 nm for the BFO film and 33 nm for the highest doped film. The substitution of Ca^{2+} for Bi^{3+} in $BiFeO_3$ can produce oxygen vacancies which apparently induce distortions and causes structural irregularities within the crystallites. Thus the local distortion and strain caused by the rhombohedral co-existing phase is reflected in physical properties of the tetragonal phase. Also, the homogeneous microstructure of BCF030 films may affect ferroelectric properties because the voltage can be uniformly applied on them.

To evaluate the role exerted by Ca on the BFO film microstructure, TEM images of pure and highly doped Ca compositions were produced. A plane-view TEM image shows the microstructure and

SAD patterns and the grain polycrystallinity in film planes. Grains are regularly shaped, and the estimated size obtained from dark field images is about 60 nm for a BFO film and 30 nm for a BCF030 film see Fig. 3a and c, respectively). Tiny pores less than 10 nm in size are present within grains and along grain boundaries. The role of Ca is to create vacancies which act as point defects and induce distortions within crystallites. Also, as the amount of Ca increases, small nucleation cores aggregate together into bigger grains and produce a smoother surface (not shown in the text). Thus, the lower grain size obtained in doped samples reflects an increase in the crystallization temperature due to differences in chemical bond strengths between Fe–O and Ca–O atoms. The $BiFeO_3$ pattern shows a rhombohedral lattice similar to the pattern previously reported for $BiFeO_3$ [35,36] while the BCF030 pattern is similar to patterns expected for a primitive cubic perovskite lattice possessing four-fold symmetry with a large tetragonal distortion within the crystal domain.

Much effort has been expended to understand resistive switching effects in metal semiconductor materials, but the mechanisms responsible for these effects are not completely understood. In this context, aside from enrolling BFO as a material candidate in this field, we would like to investigate the role of a Ca-doped BFO interface and barrier contact on resistive switching effects. Au is the top electrode in both samples forming ohmic contact. However, the bottom electrode (Pt) has a different work function, and contact barriers at bottom electrode/film interfaces are different because Pt forms a Schottky contact which could be causing different screen electric fields at the bottom electrode/film interface. Thus, the formation of the Schottky contact increases the difference between low and high resistance states as a consequence of an increase in the current flow in the forward voltage which

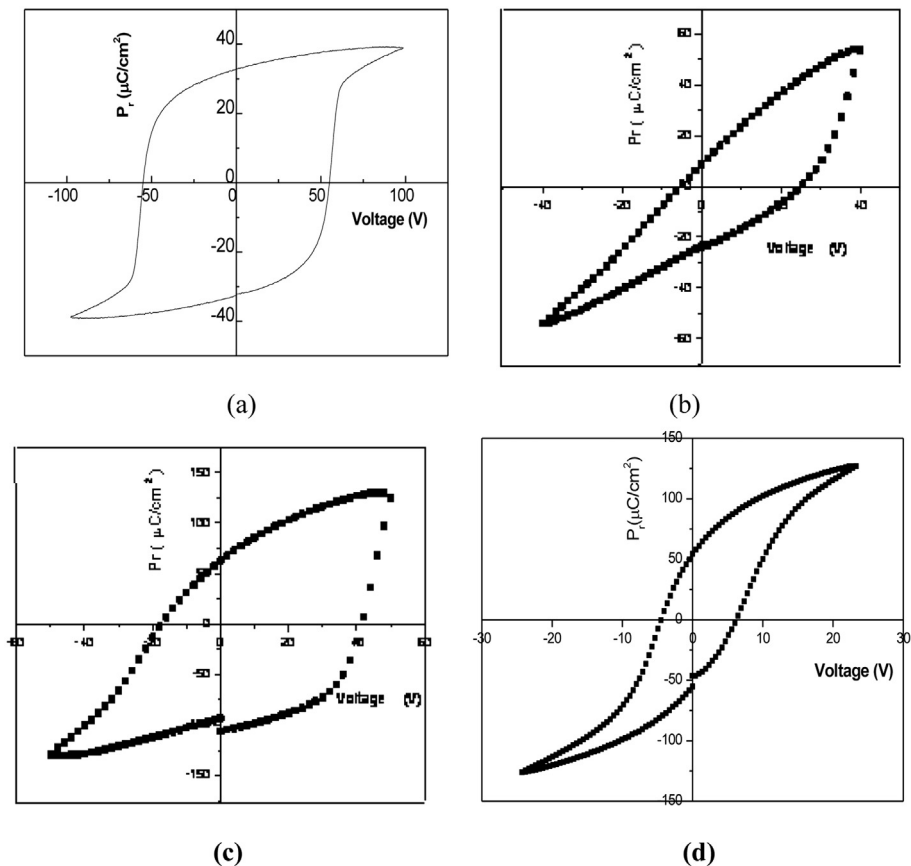


Fig. 5. Hysteresis loop of thin films deposited by the polymeric precursor method and annealed at 500 °C in static air for 2 h. (a) BFO, (b) BFOCa010, (c) BFOCa020 and (d) BFOCa030.

results in a shift in the hysteresis loop and an enhanced resistive switching effect. Our results clearly indicate that the resistive switching effect in BFO thin films is influenced by the barrier contact and the work function difference between BFO and Ca-doped BFO and electrodes where metal electrodes with high work function values forming Schottky contacts can produce increased hysteresis. In general, Schottky contacts in BFO films may be beneficial for the electronic charge transport in resistance random access memory applications. Current–voltage characteristics of the BFO and Ca-doped BFO samples were performed at room temperature with a current compliance limited to 10 μA in the measurement unit (see Fig. 4). Plots illustrate hysteresis curves usually related to resistive switching effects and commonly observed in heterostructured ferroelectric thin films [37]. This switching mechanism as a function of polarity is an intrinsic effect, and may be related to intrinsic dipole formation and/or to trap state relaxation [38]. It is observed that BFO films have a larger decrease of this effect while BCFO30 films maintain this effect because Ca inhibits grain growth. Clear I – V hysteresis is observed and is replicated reversibly. This huge difference between the measured conductivity and the estimated ionic conductivity suggests that the main carrier type which produces observed transport behavior must be electronic rather than ionic in nature. This hysteretic I – V shape can potentially be used for a resistive memory device.

Room temperature P – E hysteresis loops of BFO and Ca-doped BFO films are shown in Fig. 5. The BFO loop is well saturated and rectangular with a $P_r \sim 51 \mu\text{C}/\text{cm}^2$ under a voltage of 50 V. No sign of leakage has been observed under this measuring frequency. Liu et al. [39] reported substantially reduced leakage of BiFeO_3 films by introducing a LaNiO_3 intermediate layer. Although a saturated hysteresis loop was observed, they obtained only a remnant

polarization of $26.9 \mu\text{C}/\text{cm}^2$ under $1.25 \text{ MV}/\text{cm}^{-1}$. To our knowledge, very few reports on a large P_r and a rectangular loop of BFO film obtained from chemical methods [40,41] have been reported. However, the hysteresis loop in our study is more saturated than some BFO films on the Pt bottom electrode by the CSD method [42]. In fact, pure BFO film loops on the Pt bottom electrode are unsaturated in some cases. Gonzalez et al. [25] observed saturated hysteresis loops at room temperature in pure BFO films on a Pt bottom electrode while they observed only a small remnant polarization $\sim 36 \mu\text{C}/\text{cm}^2$ under $800 \text{ kV}/\text{cm}^{-1}$. In other typical studies from Singh et al. [43], Hu et al. [44] and Uchida et al. [45], unsaturated loops were observed under 10 kHz at room temperature. Our results are comparable to results observed in epitaxial BFO films on a (1 0 0) SrTiO_3 substrate prepared by the PLD method. The film possesses well saturated hysteresis characteristics with a remnant polarization (P_r) of $31 = \mu\text{C}/\text{cm}^2$ and a coercive field (E_c) of $560 \text{ kV}/\text{cm}^{-1}$ at a maximum applied electric field of $1000 \text{ kV}/\text{cm}^{-1}$. According to Wang et al. [46], the BFO ferroelectricity originates from relative displacements of a Bi ion and a Fe–O octahedron along the (111) orientation in epitaxial BFO thin films, and the projection polarization along the (110) orientation is larger than the (100) orientation polarization. We claim that Ca decreases the remnant polarization and stabilizes the charged domain walls which interact with oxygen vacancies and reduce the coercive field. Imprint phenomena which cause a significant shift along the electric field axis toward the positive side is also evident in low and middle Ca-doped BFO as a consequence of oxygen vacancy accumulation near the electrode-film interface which reduces the effective applied electric field. A symmetric BCFO30 curve probably originates from the local distortion and strain caused by the rhombohedral co-existing phase and is reflected in physical

properties of the tetragonal phase. Adding Ca^{2+} ions to BFO in high concentrations requires charge compensation which can be achieved by the formation of Fe^{4+} or oxygen vacancies. If Fe^{4+} exists, the statistical distribution of Fe^{3+} and Fe^{4+} ions in the octahedron may also lead to strong polarization while high coercivity can be caused by the pinning of ferroelectric domain walls which results from the ferroelectric anisotropy.

Domain structures observed in the film by piezoelectric force microscopy (PFM) are illustrated in Fig. 6. Out-of-plane (OP) and in-plane (IP) piezoresponse images of as-grown films after applying a bias of -12 V on an area of $2\text{ }\mu\text{m} \times 2\text{ }\mu\text{m}$, and then an opposite bias of $+12\text{ V}$ in the central $1\text{ }\mu\text{m} \times 1\text{ }\mu\text{m}$ area were employed. For comparison, the film topography was also analyzed (see Fig. 6a and d). To obtain domain images of the films, a high voltage that exceeds the coercive field was applied during scanning. The contrast in these images is associated with the direction of the polarization [25]. The PFM image indicates that the perpendicular component of polarization can be switched between two stable states: bright and dark contrast inside and outside of the square region. Higher PFM magnification images confirm that regions without a piezoresponse exhibit a strong contrast in PFM images. White regions in out-of-plane PFM images correspond to domains with the polarization vector oriented toward the bottom electrode (down polarization) (see Fig. 6b and e) while the dark regions correspond to domains oriented upward (up polarization). Grains which exhibit no contrast change are associated with zero out-of-plane polarization. A similar situation was observed when a positive bias was

applied to the film. We noticed that some grains exhibit a white contrast associated with a component of the polarization pointing toward the bottom electrode. On the other hand, in the in-plane PFM images (see Fig. 6c and f), the contrast changes are associated with changes in the in-plane polarization components. In this case, the white contrast indicates polarization (e.g., in the positive direction of the y -axis) while the dark contrast is given by in-plane polarization components pointing to the negative part of the y -axis. Ferroelectric domains in the BFO film consist of a multiple domain state in a mixture of 71° and 180° domains which largely grow into blocks. Domains grow in multiple states as a consequence of film thicknesses close to 350 nm. The main differences in the OP and IP piezoresponse images may be understood as follows: First, the piezoelectric tensor for the rhombohedral symmetry is complex which results in an effective piezoelectric coefficient that is not proportional to the polarization component along the detection direction as explained in Ref. [47]. In this scenario, the IP response may not change its sign upon polarization switching while the OP response does change its sign. Second, the 180° switching process may take place via two non- 180° (i.e., 71° and/or 109°) [48] switching steps which also implies switching of only one component of electrical polarization. Piezoelectric properties are improved by Ca content due to the strain energy and pinning effects which can be caused by BFO crystal structure modifications for a primitive cubic perovskite lattice with four-fold symmetry and a large tetragonal distortion within the crystal domain which affects ferroelectric and piezoelectric properties. The main difference in

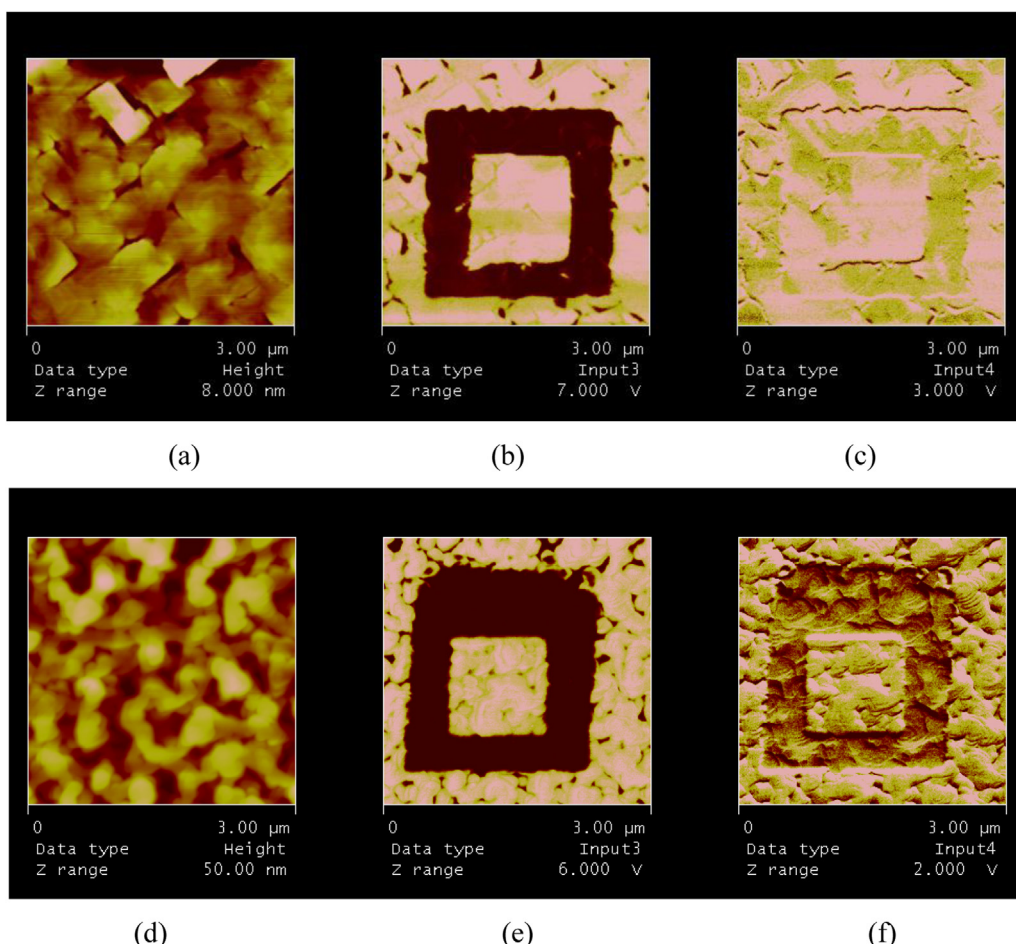


Fig. 6. Topography (TP), out-of-plane (OP) and in-plane (IP) PFM images of thin films deposited by the polymeric precursor method and annealed at $500\text{ }^\circ\text{C}$ for 2 h: (a) BFO (TP), (b) BFO (OP), (c) BFO (IP), (d) BFOCa030 (TP), (e) BFOCa030 (OP) and (f) BFOCa030 (IP).

ferroelectric and piezoelectric results is caused by the contribution of leakage current in hysteresis loops which is absent in the piezoresponse image mainly due to the effect of piezoelectric domains. Further studies are necessary to comprehend polarization switching in this system.

4. Conclusions

In summary, the effect of divalent-ion-Ca doping on multiferroic BiFeO₃ films was investigated on a Pt substrate using the soft chemical method through annealing at 500 °C for 2 h. The highest Ca concentration changes the local distortion and strain caused by the rhombohedral co-existing phase which is reflected in physical properties of the system. Among these films studied, the BCFO30 film exhibited a better microstructure, leakage current density behavior, a good *P-E* loop and strong piezoelectric characteristics. In addition, a comparative study shows that A-site Ca doping with various contents have notable influences on electrical properties, including leakage current and ferroelectric and piezoelectric properties of BFO films which may be related to modification of the structure and elimination of charge defects due to A-site Ca doping. Results of these studies are very promising and suggest that BCFO30 thin films can be used as storage elements in non-volatile ferroelectric random access memories.

Acknowledgments

The financial support of this research project by the Brazilian research funding agencies CNPq and FAPESP is gratefully acknowledged.

References

- [1] J. Wang, J.B. Neaton, H. Zheng, V. Nagarajan, S.B. Ogale, B. Liu, D. Viehland, V. Vaithyanathan, D.G. Schlom, U.V. Waghmare, N.A. Spaldin, K.M. Wuttig, R. Ramesh, *Science* 299 (2003) 1718.
- [2] W. Eerenstein, F.D. Morrison, J. Dho, M.G. Blamire, J.F. Scott, N.D. Mathur, *Science* 307 (2005) 1203.
- [3] L.W. Martin, S.P. Crane, Y.H. Chu, M.B. Holcomb, M. Gajek, M. Huijben, C.H. Yang, N. Balke, R. Ramesh, *J. Phys. C Condens. Matter.* 20 (2008) 434220.
- [4] G. Catalan, J.F. Scott, *Adv. Mater.* 21 (2009) 2463.
- [5] K.F. Wang, J.M. Liu, Z.F. Ren, *Adv. Phys.* 58 (2009) 321.
- [6] G.A. Smolenskii, I.E. Chupis, *Sov. Phys. Usp.* 25 (1982) 475.
- [7] I. Sosnowska, T. Peterlin-Neumaier, E. Steichele, *J. Phys. C Condens. Matter.* 15 (1982) 4835.
- [8] C. Ederer, N.A. Spaldin, *Phys. Rev. B* 71 (2005) 060401.
- [9] X.D. Qi, J. Dho, R. Tomov, M.G. Blamire, J.L. MacManus-Driscoll, *Appl. Phys. Lett.* 86 (2005) 062903.
- [10] F.Z. Huang, X.M. Lu, W.W. Lin, X.M. Wu, Y. Kan, J.S. Zhu, *Appl. Phys. Lett.* 89 (2006) 242914.
- [11] B.F. Yu, M.Y. Li, J. Liu, D.Y. Guo, L. Pei, X.Z. Zhao, *J. Phys. D Appl. Phys.* 41 (2008) 065003.
- [12] Y. Wang, C.W. Nan, *J. Appl. Phys.* 103 (2008) 024103.
- [13] J. Liu, M.Y. Li, L. Pei, B.F. Yu, D.Y. Guo, X.Z. Zhao, *J. Phys. D Appl. Phys.* 42 (2009) 115409.
- [14] J. Liu, M.Y. Li, L. Pei, J. Wang, B.F. Yu, X. Wang, X.Z. Zhao, *J. Alloys Compd.* 493 (2010) 544.
- [15] A. Lahmar, S. Habouti, M. Dietze, C.-H. Solterbeck, M. Es-Souni, *Appl. Phys. Lett.* 94 (2009) 012903.
- [16] Y. Wang, C.W. Nan, *Ferroelectrics* 357 (2007) 172.
- [17] H. Naganuma, J. Miura, S. Okamura, *Appl. Phys. Lett.* 93 (2008) 052901.
- [18] P. Kharel, S. Talebi, B. Ramachandran, A. Dixit, V.M. Naik, M.B. Sahana, C. Sudakar, R. Naik, M.S.R. Rao, G. Lawes, *J. Phys. C Condens. Matter.* 21 (2009) 036001.
- [19] J. Liu, M.Y. Li, L. Pei, J. Wang, Z.Q. Hu, X. Wang, X.Z. Zhao, *Europhys. Lett.* 89 (2010) 57004.
- [20] G.L. Yuan, S.W. Or, *J. Appl. Phys.* 100 (2006) 024109.
- [21] C.-H. Yang, J. Seidel, S.Y. Kim, P.B. Rossen, P. Yu, M. Gajek, Y.H. Chu, L.W. Martin, M.B. Holcomb, Q. He, P. MakSYMovich, N. Balke, S.V. Kalinin, A.P. Baddorf, S.R. Basu, M.L. Scullin, R. Ramesh, *Nature* 8 (2009) 485.
- [22] M. Fiebig, *J. Phys. D*, 38 (2005) R123.
- [23] R. Ramesh, N.A. Spaldin, *Nat. Mater.* 6 (2007) 21.
- [24] S.W. Cheong, M. Mostovoy, *Nat. Mater.* 6 (2007) 13.
- [25] A.Z. Simões, A.H.M. Gonzalez, L.S. Cavalcante, C.S. Riccardi, E. Longo, J.A. Varela, *Appl. Phys. Lett.* 90 (2007) 052906.
- [26] R.A. Young, A. Sakthivel, T.S. Moss, C.O. Paiva-Santos, *DBWS*-* an upgrade of the *DBWS** programs for Rietveld refinement with PC and mainframe computers, *J. Appl. Crystallogr.* 28 (1995) 366–367.
- [27] H.M. Rietveld, *J. Appl. Cryst.* 2 (1969) 65.
- [28] D.L. Bish, J.E. Post, *Am. Mineral.* 78 (1993) 932.
- [29] <http://www.ing.unitn.it/maud/index.html>.
- [30] L. Lutterotti, S. Matthies, H.-R. Wenk, A.J. Schultz, J.J. Richardson, *Appl. Phys.* 81 (1997) 594.
- [31] G. Will, *Powder Diffraction: The Rietveld Method and the Two Stage Method to Determine and Refine Crystal Structures from Powder Diffraction Data*, Springer-Verlag, Berlin, Heidelberg, 2006, pp. 44–69.
- [32] T. Barth, G. Lunde, *Z. Physiol. Chem.* 121 (1926) 78.
- [33] C. Lepoittevin, S. Malo, N. Barrier, N. Nguyen, G. Van. Tendeloo, M. Hervieu, *J. Solid State Chem.* 181 (2008) 2601.
- [34] S.K. Singh, K. Maruyama, H. Ishiwara, *J. Phys. D Appl. Phys.* 40 (2007) 2705.
- [35] J.K. Kim, S.S. Kim, W.J. Kim, *Integr. Ferroelectr.* 76 (2005) 103.
- [36] Y. Huang, K. Zhao, H.B. Lu, K.J. Jin, M. He, Z.H. Chen, Y.L. Zhou, G.Z. Yang, *Appl. Phys. Lett.* 88 (2006) 061919.
- [37] P.R. Bueno, R. Tararan, R. Parra, E. Joanni, M.A. Ramírez, W.C. Ribeiro, E. Longo, J.A. Varela, *J. Phys. D Appl. Phys.* 42 (2009) 055404.
- [38] X.J. Luo, C.P. Yang, S.S. Chen, X.P. Song, H. Wang, K. Barner, *J. Appl. Phys.* 108 (2010) 014107.
- [39] H. Liu, Z. Liu, K. Yao, *J. Sol-Gel. Sci. Technol.* 41 (2007) 123.
- [40] X.J. Meng, J.G. Cheng, J.L. Sun, H.J. Ye, *J. Cryst. Growth* 220 (2000) 100.
- [41] W. Zhu, M.S. Tse, W. Lu, *Integr. Ferroelectr.* 12 (1996) 167.
- [42] J.K. Kim, S.S. Kim, W. Kim, *J. Appl. Phys. Lett.* 88 (2006) 132901.
- [43] S.K. Singh, H. Ishiwara, K. Maruyama, *Appl. Phys. Lett.* 88 (2006) 262908.
- [44] G.D. Hu, X. Cheng, W.B. Wu, C.H. Yang, *Appl. Phys. Lett.* 91 (2007) 232909.
- [45] H. Uchida, R. Ueno, H. Funakubo, S. Koda, *J. Appl. Phys.* 100 (2006) 014106.
- [46] Y. Wang, C.W. Nan, *Appl. Phys. Lett.* 89 (2006) 052903.
- [47] C. Harnagea, A. Pignolet, M. Alexe, D. Hesse, *Integr. Ferroelectr.* 44 (2002) 113.
- [48] F. Zavaliche, P. shafer, R. Ramesh, M.P. Cruz, R.R. Das, D.M. Kim, C.B. Eom, *Appl. Phys.* 87 (2005) 252902.